

# A novel method for simulating smoldering propagation and its application to STAR (Self-sustaining Treatment for Active Remediation)

Stephanie L. MacPhee<sup>a</sup>, Jason I. Gerhard<sup>a,\*</sup>, Guillermo Rein<sup>b</sup>

<sup>a</sup> Department of Civil and Environmental Engineering, The University of Western Ontario, London, ON N6A 5B9, Canada

<sup>b</sup> School of Engineering, The University of Edinburgh, Edinburgh EH9 3JL, United Kingdom

## ARTICLE INFO

### Article history:

Received 9 September 2010

Received in revised form

8 November 2011

Accepted 13 November 2011

Available online 23 December 2011

### Keywords:

Smoldering propagation

Site remediation

Multiphase flow

NAPLs

Subsurface heterogeneity

## ABSTRACT

This work presents the development and proof of concept of a phenomenologically-based numerical model capable of simulating the expansion of a smoldering front in a heterogeneous reactive porous medium. This practical tool has potential for investigating a range of large-scale smoldering phenomena including subsurface peat and coal fires. The model is applied to the smoldering of non-aqueous phase liquids (NAPLs) embedded in soil. NAPLs are industrial chemicals found extensively polluting the subsurface and their in situ destruction via smoldering combustion is a promising site remediation approach referred to as STAR (Self-sustaining Treatment for Active Remediation). The In Situ Smoldering Model was developed through the novel coupling of a multiphase flow simulator with a combustion front expansion model, linked at the local (i.e., nodal) scale by a calibrated expression for the forward smoldering front velocity that is a function of airflow velocity and NAPL content. Numerical testing revealed that the model is computationally efficient and capable of handling two-dimensional smoldering propagation for a range of challenging physical scenarios.

© 2011 Elsevier Ltd. All rights reserved.

## 1. Introduction

Smoldering is a slow, low-temperature, flameless form of combustion, sustained by the heat evolved when oxygen directly attacks the surface of a condensed-phase fuel (Ohlemiller, 1985, 2002; Rein, 2009). Smoldering is a fundamental combustion problem involving heterogeneous chemical reactions and the transport of heat, mass and momentum in the gas and solid phases.

Smoldering ignition of a reactive media requires the supply of heat to the surrounding fuel. The subsequent temperature increase, first sets off thermal-degradation reactions, mainly endothermic pyrolysis, and then exothermic oxidation reactions, until the net heat released is high enough to balance the heat required for propagation (Rein, 2009). This net heat released by the reactions is partially transferred by conduction, convection and radiation ahead of the reaction and partially lost to the environment. Once ignition occurs, the smoldering reaction advances gradually through the material. The oxidizer is transported to the reaction zone by diffusion and convection (both natural and forced), feeding the oxidation reactions.

There are two modes of propagation, forward and opposed. In forward, the pyrolysis front is located at the leading edge of the reaction front since it does not need oxygen but only heat transfer to permeate into the media. The oxidation reaction takes place at the trailing edge of the reaction front, where the oxygen supply is available, and the heat released is transferred ahead of the front into the virgin fuel and pyrolysis front to drive propagation (Rein et al., 2007).

Self-sustained smoldering propagation is controlled by two main mechanisms: availability of oxygen at the combustion front and heat losses to the surroundings (Rein, 2009). Smoldering is said to be self-sustaining when, after an initial input is supplied as ignition energy, the process becomes established and produces sufficient heat to sustain the propagation unassisted by an ignition source.

Smoldering combustion has been studied most extensively with respect to polyurethane foams (e.g., Torero and Fernandez-Pello, 1995; Bar-Ilan et al., 2005; Rein, 2005; Rein et al., 2007) due to their high relevance in residential fire safety, and cellulosic materials (e.g., Ohlemiller, 1985; Kashiwagi and Nambu, 1992) due to their simple degradation chemistry. Other contexts include underground coal gasification and waste incineration. Smoldering mega-fires of coal and peat deposits, common natural phenomena, are other important areas of study due to their destruction of ecosystems and large contribution to global carbon emissions (Rein, 2009). These fires burn for extended periods of time (months to years) due to their

\* Corresponding author.

E-mail address: [jgerhard@uwo.ca](mailto:jgerhard@uwo.ca) (J.I. Gerhard).

self-sustaining nature, and can propagate deep into the subsurface if a supply of oxygen is available (e.g., cracks, channels, galleries) (Rein, 2009). Most studies focus on smoldering of porous reactive solids with very few considering smoldering of reactive liquids within an inert porous matrix (Akkutlu and Yortsos, 2003; Pironi et al., 2009).

Non-Aqueous Phase Liquids (NAPLs) represent one of the most prevalent and problematic classes of industrial compounds polluting the environment (Pankow and Cherry, 1996). Common lighter-than-water NAPLs (LNAPLs) include gasoline, diesel, jet fuel, and fuel oil, while denser-than-water NAPLs (DNAPLs) include coal tar, crude oil, creosote, chlorinated solvents, and polychlorinated biphenyl (PCB) oils. In particular, compounds with more complex structures, such as creosote and coal tar, are highly recalcitrant and thus very difficult to remediate with technologies currently available (National Research Council, 2004).

Switzer et al. (2009) proposed a novel remediation approach – known as STAR (Self-sustaining Treatment for Active Remediation) – based on the smoldering of NAPLs. NAPL destruction (i.e., clean-up) via self-sustained smoldering was demonstrated by Switzer et al. (2009) across a range of experimental conditions (e.g., varying soil types, contaminant types) via proof-of-concept experiments. Pironi et al. (2011) presented a detailed set of column experiments examining the sensitivity of the process (smoldering front velocity and maximum temperature) to key parameters (inlet air flux and contaminant concentration) for coal tar in sand. Those studies provide key calibration and validation data for any model developed for simulating the process. Numerical models are valuable tools that are widely employed by environmental engineers for designing and optimizing field-scale remediation systems (Pankow and Cherry, 1996).

Explicit numerical simulation of smoldering behavior presents a significant challenge due to the general lack of availability of the kinetic parameters associated with the combustion and thermal decomposition of most smoldering fuels, and uncertainties associated with the coupled chemical and physical processes involved in the generation and transport of heat and mass (Rein, 2005). Thus, most fundamental models are physically based but consider only the one-dimensional case, and are computationally very intensive, even for simulations at the scale of tens of centimeters (Rein et al., 2007).

An alternative approach is the development of simple analytical models based on global energy and mass balances at the reaction front to predict steady-state, one-dimensional forward and opposed propagation (Torero and Fernandez-Pello, 1995; Rein, 2009). These take advantage of the fact that self-sustained propagation of a smoldering front is governed by the flow of oxygen to the front and heat losses to the surroundings (Rein, 2009). Models developed within this framework typically provide an analytical expression for the steady-state velocity of the smoldering front given the oxygen flux and known thermo-chemical parameters, such as the effective heat and peak temperature of smoldering of the fuel, effective stoichiometry (i.e., the amount of oxygen necessary to oxidize 1 kg of fuel) and the overall heat capacity of the porous bed. This global approach could be applied at the local scale (i.e., centimeters) when the oxygen flux and fuel conditions are relatively homogeneous, but alone is insufficient to reliably predict propagation in larger domains where heterogeneous conditions (e.g., oxygen flux depends on porous media permeability and fuel content) are expected. The effective simulation of smoldering propagation at the field scale (i.e., hundreds of meters) requires yet an approach different from the fundamental physical–chemical and the global balance models.

A similar challenge is faced in the simulation of wildfires spreading over large forest domains (kilometers long). Simple and fast models have been developed to track the propagation of the fire

front over a two-dimensional forest based on Huygens' Principle (e.g., Anderson, 1983; Richards, 1990, 1993, 1995; Knight and Coleman, 1993; Coleman and Sullivan, 1996; Finney, 1998). This methodology, adapted for forest fire perimeter expansion modeling, exhibits some ideal characteristics for field-scale modeling of NAPL smoldering: (i) does not require detailed combustion parameterization, (ii) computationally efficient at large scales, and (iii) permits spatial heterogeneity in key data sets including airflow and fuel loading. Limitations of perimeter expansion modeling include that it relies on calibrated spread rate expressions and works well for flat, circular or elliptical front perimeters but deviation from this can prove numerically challenging. Richards (1995) also stated that the major constraints associated with this method include a low tolerance for local conditions that stray far from homogeneity. In order to increase confidence in the method, new comparisons to experimental fire data are always sought (Richards, 1995). While these models provide a framework for solving the global front expansion problem, locally they require a context-specific functional relationship between front velocity and key dependent variables (e.g., for NAPL smoldering these are fuel type, oxygen flux and fuel concentration). In the context of field-scale simulation of in situ smoldering, the spatial distribution of air velocity will evolve in time, mainly because fuel consumption affects flow permeability, and thus it needs to be calculated based on the laws for gas transport in porous media. In their review, Thomson and Johnson (2000) illustrated that multiphase flow numerical models (e.g., TETRAD, T2VOC) are able to capture the distribution of different fluid phases (e.g., air and water) in response to air injection into the subsurface.

This paper presents the development and proof of concept of a phenomenological numerical model capable of simulating the expansion of a smoldering front perimeter in NAPL-contaminated, heterogeneous porous media with potential applications to field scales. This In Situ Smoldering Model (ISSM) utilizes the novel coupling of a finite difference, multiphase (NAPL and air) flow numerical model (Gerhard and Kueper, 2003a, 2003b) with a combustion front expansion model (Richards, 1990, 1995). These models are linked at the local scale by an analytical expression for the smoldering front velocity that is a function of airflow velocity and NAPL saturation (i.e., fraction of the pore space occupied by NAPL). This expression is calibrated using the only existing set of DNAPL-smoldering experiments.

This work presents the model's development, calibration to column experiments, and evaluation of the ability of the numerical algorithm to handle simulations of NAPL-smoldering behavior for several challenging physical scenarios.

## 2. Model formulation

A schematic of the model formulation and coupling between its key components is illustrated in Fig. 1. The key components are (i) a multiphase flow model, (ii) a calibrated smoldering velocity expression, (iii) a front expansion model, (iv) front clipping and regridding routines and (v) a NAPL destruction subroutine. Each of these is described in turn below.

### 2.1. Multiphase flow model

DNAPL3D (Gerhard and Kueper, 2003a, 2003b; Gerhard et al., 1998; Grant et al., 2007; Kueper and Frind, 1991) is a three-dimensional, finite difference numerical model that simulates the flow of two immiscible fluids through porous media. DNAPL3D has been employed primarily for simulating the migration of DNAPLs in water-saturated heterogeneous porous media (e.g., Gerhard and Kueper, 2003c; Gerhard et al., 2001, 2007; Grant et al., 2007; Kueper

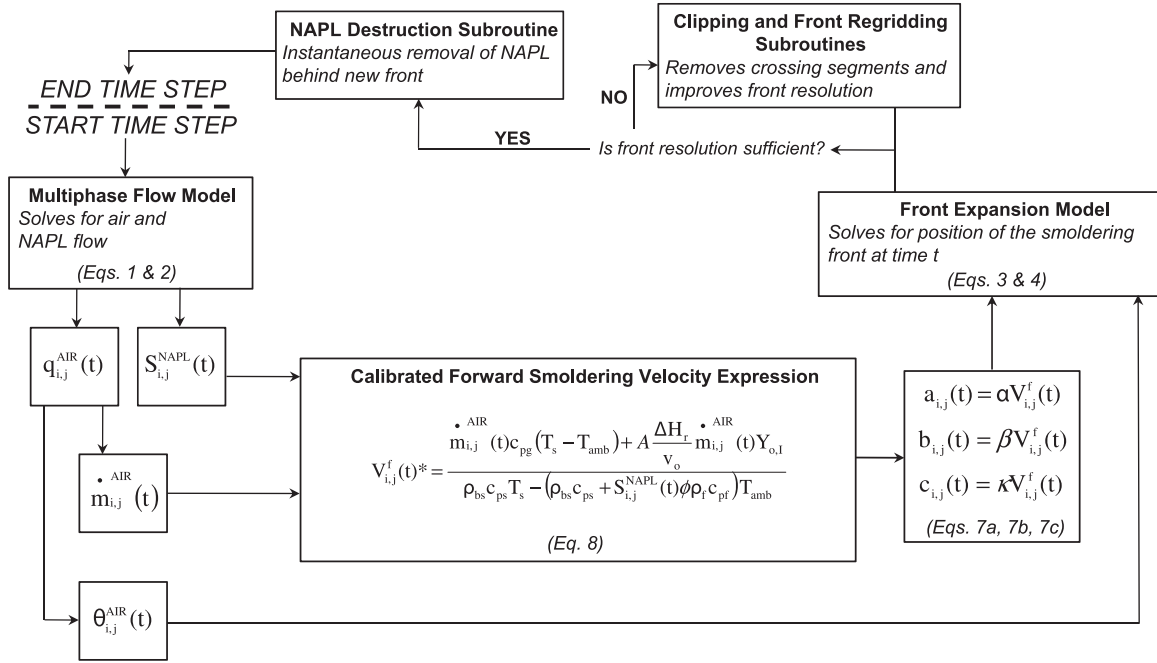


Fig. 1. Schematic process flow diagram for the In Situ Smoldering Model.

and Gerhard, 1995). In those studies, DNAPL is considered the non-wetting phase while water is considered the wetting phase (i.e., coating the soil matrix). For the purposes of this work, the model is employed to simulate the migration of NAPL and air, where NAPL is considered wetting with respect to air on the soil matrix. Mass transfer between the phases is neglected; this is considered reasonable because the focus is on the physical propagation of the smoldering front and the NAPL considered in this work (coal tar) is relatively non-volatile. We note that for some common NAPLs (e.g., chlorinated solvents), significant volatilization may be expected at elevated temperatures. However, the calibration procedure for the smoldering velocity expression (Section 2.3) will take into account any influences of NAPL mass loss to volatilization, even if the amount is not known, as long as sufficient NAPL mass remains when the front arrives at a location to sustain the smoldering reaction. Mass transfer may need to be considered for volatile NAPLs (not considered in this work) where volatilization is severe enough ahead of the front that the distribution of air flux is significantly affected.

For two-dimensional scenarios, the model solves the wetting and non-wetting phase mass conservation equations (Kueper and Frind, 1991). By substituting the multiphase extension of Darcy's Law, the capillary pressure definition  $P_C = P_N - P_W$ , and the saturation relationship  $S_{NW} + S_W = 1.0$  and assuming incompressible fluids the matrix Equations (1) and (2) are obtained (Kueper and Frind, 1991):

$$\frac{\partial}{\partial x_i} \left[ \frac{k_{ij} k_{r,W}}{\mu_W} \left( \frac{\partial P_W}{\partial x_j} + \rho_W g \frac{\partial z}{\partial x_j} \right) \right] - \phi \frac{\partial S_W}{\partial t} = 0 \quad i, j = x, y \quad (1)$$

$$\frac{\partial}{\partial x_i} \left[ \frac{k_{ij} k_{r,N}}{\mu_N} \left( \frac{\partial (P_C + P_W)}{\partial x_j} + \rho_N g \frac{\partial z}{\partial x_j} \right) \right] + \phi \frac{\partial S_N}{\partial t} = 0 \quad i, j = x, y \quad (2)$$

where  $k_{ij}$  is a second-order tensor for intrinsic permeability,  $k_{r,W}$  and  $k_{r,N}$  represent the relative permeability of the wetting and non-wetting phases, respectively,  $\mu_W$  and  $\mu_N$  represent the wetting and non-wetting phase viscosities, respectively,  $P_W$  and  $P_N$

represent the wetting and non-wetting phase pressures, respectively,  $P_C$  is the capillary pressure,  $\rho_W$  and  $\rho_N$  are the densities of the wetting and non-wetting phases respectively,  $S_W$  and  $S_{NW}$  are the wetting and non-wetting phase saturations (i.e., fluid-occupied fraction of pore space), respectively,  $g$  is gravitational acceleration,  $\phi$  is the porosity,  $t$  is time and  $x$  and  $y$  are the spatial coordinates. Equations (1) and (2) reveal that the rate of flow for each phase is proportional to its effective permeability ( $k_{ij} \times k_r$ ) and the applied hydraulic gradient i.e., (pressure and elevation head), both of which are dependent on saturation via the  $k_r(S_W)$  and  $P_C(S_W)$  constitutive relationships. It is acknowledged that the elevation head term in Equation (2) is not significant in this application since the non-wetting phase, air, has such a low density (Table 3).

Equations (1) and (2) are solved numerically using a fully implicit, seven-point, node centered, finite difference scheme with second-order accurate spatial operators and a first-order accurate temporal derivative (Rosenburg, 1969). The internode

Table 1

Pironi et al. (2011) experiments employed for model calibration.

Set of experiments	Case	NAPL type	Variable	Air flow rate (cm/s)	Initial NAPL saturation
1	1	Coal tar	Air flow rate	9.15	0.25
	2			4.05	
	3			16.6	
	4			25.2	
2	5	Coal tar	Saturation	9.15	0.10
	6				0.25
	7				0.35
	8				0.50
3	9	Crude oil	Fuel type/air flow rate	4.05	0.25
	10			9.15	
	11			16.6	
	12			25.2	
4	13	Crude oil	Fuel type/saturation	9.15	0.15
	14				0.25
	15				0.35
	16				0.50

**Table 2**  
Smoldering velocity parameters for coal tar.

Parameter	Value
Overall stoichiometric coefficient ( $v_O$ )	2.89 <sup>a</sup>
Effective heat of smoldering ( $\Delta H_f$ )	39.4 (MJ/kg) <sup>a</sup>
Specific heat of the NAPL ( $c_{NAPL}$ )	1880 (J/kg <sub>NAPL</sub> /K) <sup>b</sup>
Smoldering temperature ( $T_s$ )	1030 (K) <sup>a</sup>
NAPL density ( $\rho_{NAPL}$ )	1180 (kg/m <sup>3</sup> ) <sup>d,e</sup>
Calibration parameter ( $A$ )	0.10
Mass fraction of oxygen in the gas phase ( $Y_O$ )	0.235 (kg <sub>O<sub>2</sub></sub> /kg <sub>gas</sub> ) <sup>b</sup>
Specific heat of the gas ( $c_{pg}$ )	1100 (J/kg/K) <sup>c</sup>
Specific heat of the porous media ( $c_s$ )	1265 (J/kg/K) <sup>b</sup>

<sup>a</sup> Pironi, 2009.<sup>b</sup> Green, 2008.<sup>c</sup> Incropera and DeWitt, 1996.<sup>d</sup> Pycnometer Method (ASTM Standard).<sup>e</sup> At temperature of 20 °C.

permeabilities are calculated using harmonic means, and the internode relative permeabilities are calculated using fluid saturations at the upstream nodes (Aziz and Settari, 1972). Full Newton–Raphson iteration is employed and a modified ORTHOMIN routine is used to solve the preconditioned system (Behie et al., 1984). Constitutive functions are incorporated that have been validated in one- and two-dimensions for the flow of two immiscible phases in heterogeneous porous media (Gerhard and Kueper, 2003a, 2003b, 2003c; Grant et al., 2007).

In this work, the multiphase flow model permits simulation of air injection into a two-dimensional (cross-section) subsurface domain. The model permits a heterogeneous distribution of soil properties, and solves for the spatially and temporally evolving velocity distributions of both air and NAPL, accounting for the influence of phase density and viscosity, pressure and elevation gradients, and influence of saturation on effective permeability. The air velocity and NAPL saturation, in particular, are key parameters on which the velocity of the smoldering front depends (Pironi et al., 2011).

An assumption in this work is the incompressibility of the air phase. This is a common assumption in air sparging models (e.g., Marley et al., 1992; Philip, 1998; van Dijke and Van Der Zee, 1998; van Dijke et al., 1995). In the present range of temperature (<1100 K), pressure (<5000 Pa) and airflow velocities (<1 m/s), air

is an incompressible fluid as the Mach number is well below 0.3 (it is well known that air can be considered incompressible for Mach numbers below 0.3). While air does compress initially under typical field injection pressures, once the air injection rate has reached steady-state, compressibility of the air phase is not significant (van Dijke et al., 1995). For the systems investigated in this work, steady-state airflow is established very quickly relative to the typically low rate of smoldering propagation [figures not shown]. Similar to the model validation exercise conducted by McCray and Falta (1997), DNAPL3D was employed to simulate the air sparging experiments conducted by Ji et al. (1993) [figures not shown]. This experiment involved the injection of air at a point source into a two-dimensional, water-saturated flume packed with glass beads. Successful prediction of the air distribution pattern by DNAPL3D, very similar to that shown by McCray and Falta (1997), provided confidence in the model's ability to simulate air injection.

An explicit dependence of fluid properties (e.g., air density, NAPL viscosity) on temperature is neglected in this work. The employment of a velocity expression in the model that is calibrated to a subset of experiments effectively accounts for temperature effects around the front. The successful prediction of global propagation patterns of the smoldering front (see Section 3) suggests that this approach is adequate, at least for simulations of NAPL smoldering at the bench scale (which are the focus of this study). Physically-based smoldering modeling using the ideal gas law (Rein et al., 2007) shows that thermal expansion effects on smoldering are small and apply only a short distance downstream of the front. Thermal expansion only affects the smoldering front in the relatively small region where combustion and gas preheating take place. Downstream heating does not affect smoldering since that flow has already passed the front. It is noted that NAPL mobilization, or the influence of any mobilization on front propagation, was not observed in the experiments (Pironi et al., 2011). It is acknowledged that under some scenarios and with some NAPLs, increased mobility at elevated temperatures may be significant; additional experiments and model development would be necessary to explore this behavior.

In addition, the presence of water is not considered in this work. It is noted that there are many smoldering phenomena to which this numerical approach could be applied for which water is not a significant component, such as fires in dry peatlands, coal seams above the water table, NAPL in situ that exist above the water table, and NAPL in ex situ reactors with excavated, drained soils. Moreover, it is anticipated the modeling approach can be applied in some circumstances in the presence of water. Pironi et al. (2011) illustrates that when water saturation was varied from 0% to 75% while coal tar saturation was maintained at 25%, the velocity of the combustion front was essentially invariant. This is because the combustion reaction is exothermic enough that a relatively small fraction of the power is invested in drying the soil.

## 2.2. Smoldering front expansion model

A general mathematical framework is presented in Richards (1995) for the expansion of a forest fire front approximated by a set of geometrically-based partial differential equations. Richards' model assumes a continuous plane where the front is represented as an ellipse made up of vertices defined by  $x$  and  $y$  coordinates that expands in time. Comparison to actual fires reveals that the propagating shape of the front that had started from a single point is well approximated by an ellipse or series of ellipses (van Wagner, 1969; Anderson, 1983; Green et al., 1983). It is assumed that the maximum rate of expansion occurs along the direction of the wind (the equivalent to seepage airflow in the porous media case) and defines the major axis of the ellipse. The origin of the coordinate

**Table 3**  
Fluid and porous media simulation parameters for coal tar and air.

Fluid and soil properties	Value
Surface tension ( $\sigma$ )	0.033 (N/m) <sup>a,b</sup>
Density of air ( $\rho_{air}$ )	1.204 (kg/m <sup>3</sup> ) <sup>a,c</sup>
Air viscosity ( $\mu_{air}$ )	$1.81 \times 10^{-5}$ (Pa·s) <sup>a,c</sup>
Coal tar viscosity ( $\mu_{coal\ tar}$ )	7.59 (Pa·s) <sup>a,d</sup>
Mean particle diameter ( $\bar{d}$ )	1.295 (mm) <sup>e</sup>
Mean permeability ( $k$ )	$1.90 \times 10^{-10}$ (m <sup>2</sup> ) <sup>e</sup>
Porosity ( $\phi$ )	0.38 <sup>e</sup>
Displacement pressure ( $P_D$ )	258.0 (Pa) <sup>e</sup>
Pore size distribution index ( $\lambda$ )	3.41 <sup>e</sup>
Residual NAPL saturation ( $S_{rw}$ )	0.01
Maximum non-wetting phase residual ( $S_{nrmax}$ )	0.15
Emergence wetting phase saturation ( $S_{w-emerg}$ )	0.90
Maximum achievable non-wetting phase relative permeability ( $k_{rmax}$ )	1.0

<sup>a</sup> At temperature of 20 °C.<sup>b</sup> Pendant Drop Shape Method with an Axisymmetric Drop Shape Analyser (ADSA) (Lord et al. 2000).<sup>c</sup> Potter and Wiggert, 2001.<sup>d</sup> Brookfield DV III Rheometer.<sup>e</sup> Grant, 2005.



system is considered to be the point at which ignition occurs and is typically located at the rear focus of the ellipse (Finney, 1998).

This approach to modeling front expansion is based on Huygens' Principle which states that the variables that control the magnitude and direction of elliptical expansion are known instantaneously at each vertex and are a function of the properties of the underlying system, such as fuel content and air velocity (see Fig. 2). Many examples of the application of Huygens' Principle to the spread of fires exist in the literature (Anderson, 1983; Knight and Coleman, 1993; Richards, 1993, 1995; Richards and Bryce, 1995; Coleman and Sullivan, 1996; Finney, 1998). This approach has not been previously applied to smoldering fires; however, it is entirely reasonable because air flow velocity and fuel content are the controlling variables dictating propagation in both applications (Finney, 1998; Switzer et al., 2009; Pironi et al., 2011). Furthermore, Richards' (1990, 1995) formulation is general, permitting the functional relationship defining the front propagation to be adapted to different combustion scenarios (Richards, 1995; Richards and Bryce, 1995; Finney, 1998).

The parametric representations of the combustion perimeter and its expansion rate at a specified time ( $t$ ) following ignition are (Richards, 1990, 1995; Richards and Bryce, 1995):

$$\frac{\partial x}{\partial t} = \frac{a^2 \cos \theta \left( \frac{\partial y}{\partial s} \cos \theta - \frac{\partial x}{\partial s} \sin \theta \right) + b^2 \sin \theta \left( \frac{\partial x}{\partial s} \cos \theta + \frac{\partial y}{\partial s} \sin \theta \right)}{\sqrt{\left( \left( a \left( \frac{\partial y}{\partial s} \cos \theta - \frac{\partial x}{\partial s} \sin \theta \right) \right)^2 + \left( b \left( \frac{\partial x}{\partial s} \cos \theta + \frac{\partial y}{\partial s} \sin \theta \right) \right)^2 \right)} + c \cos \theta} \quad (3)$$

$$\frac{\partial y}{\partial t} = \frac{a^2 \sin \theta \left( \frac{\partial y}{\partial s} \cos \theta - \frac{\partial x}{\partial s} \sin \theta \right) + b^2 \cos \theta \left( \frac{\partial x}{\partial s} \cos \theta + \frac{\partial y}{\partial s} \sin \theta \right)}{\sqrt{\left( \left( a \left( \frac{\partial y}{\partial s} \cos \theta - \frac{\partial x}{\partial s} \sin \theta \right) \right)^2 + \left( b \left( \frac{\partial x}{\partial s} \cos \theta + \frac{\partial y}{\partial s} \sin \theta \right) \right)^2 \right)} + c \sin \theta} \quad (4)$$

where  $x$  and  $y$  coordinates define the front perimeter at time  $t$  and are defined sequentially at angle  $s$  to the major axis of the ellipse, where  $0 \leq s \leq 2\pi$ . The direction of the wind relative to the  $x$ -axis is represented by  $\theta$ . Ellipse dimensions are determined by variables  $a$ ,  $b$  and  $c$  where  $a \, dt$  is  $1/2$  of the major ellipse axis,  $b \, dt$  is  $1/2$  of the minor ellipse axis and  $c \, dt$  is the distance from the center of the ellipse to the ignition point located at the rear focus (see Fig. 3). The

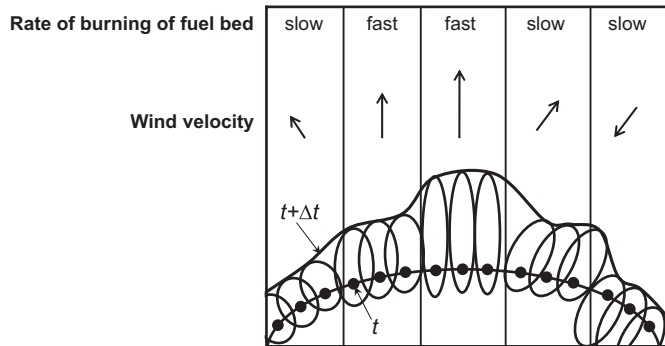


**Fig. 2.** Illustration of Huygens' Principle under heterogeneous conditions in which the fuel bed and wind velocity vary throughout the domain. As a result of spatial variations in fuel and wind conditions in the domain underlying the fire perimeter, the elliptical wavelets along the front vary in shape and orientation. The envelope surrounding the wavelets represents the position of the fire front at the subsequent time step (Finney, 1998).

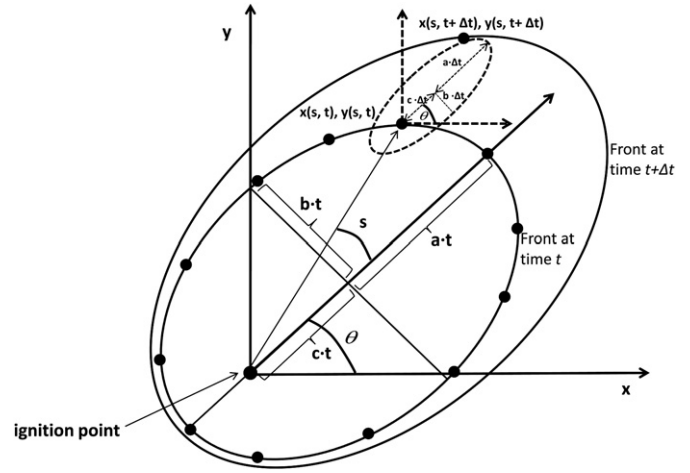


**Fig. 3.** Schematic of ellipse dimensions and parameters used in Richards' equations to solve for the position of the fire front perimeter at time  $t + \Delta t$  (after Richards, 1990).

initial condition, defined by a small ellipse that is placed at the designated ignition location ( $x_i, y_i$ ) in the solution domain, is:

$$x(s, 0) = B \cos(s) + x_i \quad (5a)$$

$$y(s, 0) = C \sin(s) + y_i \quad (5b)$$

where  $B$  and  $C$  define the initial dimensions of the ellipse. It should be noted that variables  $a$ ,  $b$ ,  $c$ ,  $x$ ,  $y$  and  $\theta$  in Equations (3) and (4) are all functions of  $s$  and  $t$  (not shown in the equations). As illustrated in Fig. 3, elliptical wavelets are computed at each origin point  $[x(s, t), y(s, t)]$  on the perimeter at time  $t$  and the envelope that surrounds the wavelets is the new front perimeter at time  $t + \Delta t$ . The distance that the front moves in a specified time step at a location is determined by the size and orientation of the local elliptical wavelet which is a function of local values of the variables  $a$ ,  $b$ ,  $c$  and  $\theta$ .

The temporal and spatial derivatives in Equations (3) and (4) are approximated by forward and central finite difference schemes, respectively, and an explicit solution is derived through substitution that generates an array of vertices representing the combustion front at time  $t$  (Richards and Bryce, 1995). The spatial derivative (central difference) is second-order accurate and the temporal derivative (forward difference) is first-order accurate.

Following Finney (1998), a clipping subroutine analyzes the predicted front and corrects instances of crossing segments along the front to avoid the formation of loops. Furthermore, a front regridding scheme, similar to the Richards (1995) algorithm, dynamically adjusts the spatial discretization along the front to ensure the front is smooth and continuous while optimizing for speed of computation. The spacing of the points along the line that represents the front is maintained to always be less than the resolution of the underlying finite difference multiphase flow grid. Furthermore, the distance between every other point on the front is tested and if this distance is less than half of the grid discretization then a point is removed. The effect of the regridding scheme on the shape and continuity of the front is illustrated in Section 4.2.

Variables  $a$ ,  $b$ ,  $c$  and  $\theta$  are characterized by the local conditions occurring instantaneously at each point along the perimeter. The local forward, lateral and opposed spread rates, respectively are defined as (Richards, 1990, 1995):

$$V_{ij}^f(t) = a_{ij}(t) + c_{ij}(t) \quad i, j = x, y \quad (6a)$$

$$V_{ij}^l(t) = b_{ij}(t) \quad i, j = x, y \quad (6b)$$

$$V_{ij}^o(t) = a_{ij}(t) - c_{ij}(t) \quad i, j = x, y \quad (6c)$$

in which variables  $a$ ,  $b$  and  $c$  (same as those defined in Equations (3) and (4)) have a unique value for each multiphase flow grid node ( $i, j$ ) and vary with time. After rearranging and substitution of Equations (6a)–(6c), variables  $a$ ,  $b$  and  $c$  are solved for in terms of  $V_{ij}^f(t)$  such that all three variables are linearly related to the forward spread rate:

$$a_{ij}(t) = \alpha V_{ij}^f(t) \quad (7a)$$

$$b_{ij}(t) = \beta V_{ij}^f(t) \quad (7b)$$

$$c_{ij}(t) = \kappa V_{ij}^f(t) \quad (7c)$$

where  $\alpha$ ,  $\beta$  and  $\kappa$  are constants. Rein et al. (2007) illustrated, via modeling of polyurethane foam smoldering, that the velocity of opposed smoldering is typically 0.75 times that of forward smoldering (Rein et al., 2007). Due to the lack of any other source of data, it is assumed here that the foam opposed value applies to NAPL and that the lateral smoldering velocity is the average of the forward and opposed propagation rates. Employing these assumptions provides  $\alpha$ ,  $\beta$  and  $\kappa$  equal to 0.875, 0.875 and 0.125, respectively.

As noted in the introduction, smoldering is characterized by multiple reactions: pyrolysis travels with the heat transfer front while the oxidation front speed depends also on the oxygen availability (Rein et al., 2006). The ISSM assumes that both fronts propagate at the same velocity and are co-located. From data on forward smoldering of synthetic foams, this is known to be a good approximation for large domains since the pyrolysis front propagates only slightly ahead of the oxidation front (Rein et al., 2007).

### 2.3. Calibration of the smoldering velocity expression

Parameters  $a$ ,  $b$ , and  $c$  – and thus  $V_{ij}^f(t)$  – are typically based on experimental data such that the shape and rate of expansion of the front will have a functional dependence on fuel type, fuel amount, and air velocity (Richards, 1995). In this work, the influence of these three parameters on  $V_{ij}^f(t)$  is incorporated via an analytical expression for the forward smoldering velocity based on a global energy balance at the front scale (Rein, 2009; Pironi, 2009). Furthermore, that expression is calibrated to the experimental data of Pironi et al. (2011) in order to extract the effective parameters and observed behavior for the DNAPL of interest.

Table 1 presents the four sets of one-dimensional, self-sustaining coal tar and crude oil smoldering experiments of Pironi et al. (2011) employed herein for model calibration. Experiments were carried out in quartz glass columns 275 mm in height and 138 mm in diameter and a standard column packing method was employed: (i) A thin layer of clean sand was placed at the bottom of the column followed by the placement of a planer air injection manifold (covering the entire base of the column) followed by a layer of clean sand upon which the igniter was positioned; (ii) A thick layer of NAPL-embedded sand was then emplaced in the column followed by another layer of clean sand; (iii) The igniter, composed of a metal heating coil wound in a flat spiral covering the entire horizontal cross-section of the column, was placed near the bottom of the column to promote forward propagation of the smoldering front up the column; (iv) An air injection manifold was then employed throughout the experiment to achieve self-sustaining smoldering propagation in an axisymmetric configuration. Additional details of

the methods and materials for these experiments are presented in Switzer et al. (2009), Pironi (2009), Pironi et al. (2009) and Pironi et al. (2011).

In previous studies (Rein, 2009; Torero and Fernandez-Pello, 1996), the forward velocity of a propagating smoldering front was predicted using an analytical expression derived from global energy conservation. A similar analytical expression was employed by Pironi (2009) for the forward smoldering front velocity for NAPLs in porous media using identical assumptions: (i) constant gas mass flux, (ii) gas velocity much greater than the velocity of the smoldering front, (iii) all oxygen is consumed at the reaction front, (iv) adiabatic conditions, and (v) steady-state energy balance. In Torero and Fernandez-Pello (1996), the analytical model results showed a good fit with experimental results for the prediction of self-sustained forward smoldering velocity following the adjustment of the parameters related to the effective heat of smoldering and stoichiometry. The analytical model employed by Pironi (2009) predicts the general trends of the experimental data – suggesting that the relationships between key variables is captured – but overpredicts the magnitude of the forward velocity for NAPL-smoldering experiments. Therefore, a similar adjustment of the parameters related to the heat of smoldering and stoichiometry was made in this work such that Equation (8) was modified to permit calibration to existing laboratory data:

$$V_{ij}^f(t) = \frac{\dot{m}_{ij}^{AIR}(t) c_{Pg} \left( T_s - T_{amb} \right) + A \frac{\Delta H_r}{v_O} \dot{m}_{ij}^{AIR}(t) \cdot Y_{O,I}}{\left( \rho_{bs} c_{ps} T_s - \left( \rho_{bs} c_{ps} + S_{ij}^{NAPL}(t) \phi \rho_{NAPL} c_{pNAPL} \right) T_{amb} \right)} \quad i, j = x, y \quad (8)$$

where  $\dot{m}_{ij}^{AIR}(t)$  is the gas mass flux,  $c_{ps}$ ,  $c_{pNAPL}$  and  $c_{pg}$  are the specific heat constants for the solid, NAPL and gas phases, respectively,  $T_s$  and  $T_{amb}$  are the peak smoldering front temperature and the ambient system temperature, respectively,  $\Delta H_r$  represents the effective heat of smoldering,  $v_O$  is the oxygen/fuel overall stoichiometric coefficient,  $Y_{O,I}$  is the initial mass fraction of oxygen present in the gas phase,  $\rho_{bs}$  is the bulk density of the solid,  $\rho_{NAPL}$  represents the density of the NAPL phase,  $S_{ij}^{NAPL}(t)$  represents the NAPL saturation,  $\phi$  represents the soil porosity,  $t$  is time and  $A$  is the calibration parameter determined by minimizing the Root Mean Square Error (RMSE) between predicted and experimental results for each set of experiments and is specific to each fuel type. Table 2 lists the parameters used in the calibrated forward smoldering velocity expression (Equation (8)). An average smoldering front temperature has been employed for  $T_s$  which is fuel specific and is a representative temperature for all the Pironi et al. (2011) experiments. It is noted that the results are not sensitive to this assumption because the calibration parameter  $A$  would absorb any changes to the smoldering temperature.

Results from Pironi et al. (2011) experimental set #1 (Cases 1–4, Table 1) for an initial coal tar saturation of 25% in which the air injection rate was varied are compared with calibrated results from Equation (8) (Fig. 4). As demonstrated by Pironi et al. (2011), the smoldering velocity increases linearly with an increase in air flux, as predicted by the theoretical energy balance Eq. (8). The critical airflow below which there is no propagation has not been experimentally determined, but it is assumed in this work to be 0.5 cm/s (the lowest value tested); below this value the smoldering front is assigned zero velocity in the ISSM. The calibration value of 0.10 for  $A$  gives a RMSE between the experiments and calibration is 0.13 cm/min. Results from Pironi et al. (2011) experimental set #2 (Cases 5–8, Table 1), in which an air injection rate of 9.15 cm/s is applied across a range of initial coal tar saturations, are compared with calibrated results (Fig. 5). It is demonstrated that above the critical

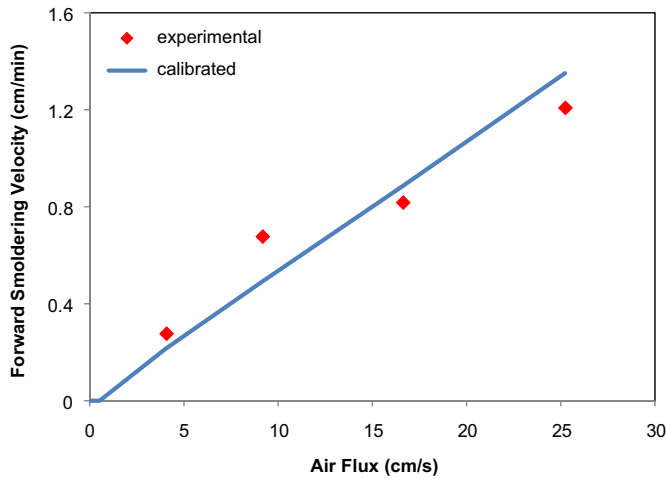


**Fig. 4.** Calibration experimental set 1 – comparison between calibrated and experimental results (Pironi et al., 2011) across a range of air injection rates with an initial coal tar saturation of 25%. The critical airflow for propagation is 0.5 cm/s.

DNAPL saturation of 0.1, and within the range up to 0.5, the forward smoldering velocity is weakly dependent on saturation (RMSE is 0.10 cm/min). Note that although the smoldering velocity does not depend strongly on saturation, Pironi (2009) shows that DNAPL pyrolysis, which is driven by the thermal front, is strongly linked to saturation. The identification of the critical airflow and saturation below which self-sustained propagation is not possible are essential elements for the field scale application of the ISSM. This information can only be obtained from experiments and is imposed on the calibrated expression.

Results for experimental sets #3 and #4 (cases 9–12 and cases 13–16, respectively, Table 1) which examine the influence of airflow and saturation on the smoldering velocity in crude oil-contaminated sand, are similar to Figs. 4 and 5 (figures not shown). The smoldering velocity increases linearly with an increase in airflow, and is weakly dependent on NAPL content. The calibration value of 0.05 for  $A$  gives RMSE values of 0.14 cm/min and 0.06 cm/min, respectively.

All together, these results illustrate that the calibrated expression (Equation (8)) follows the observed NAPL smoldering front

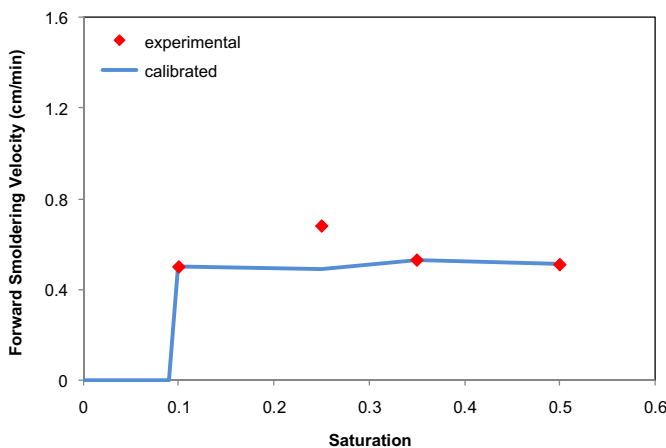


**Fig. 5.** Calibration experimental set 2 – comparison between calibrated and experimental results (Pironi et al., 2011) across a range of initial coal tar saturations with constant air injection velocity of 9.15 cm/s. The critical minimum fuel saturation for propagation is taken as 10%, the lowest value for which self-sustaining behavior was observed.

velocities across a wide range of experimental conditions for two different NAPLs. Furthermore, the calibrated expression permits the computation of front velocities for any combination of these independent variables by assuming that the dependence of the front velocity on air flux is independent of NAPL content and vice versa. This remains to be confirmed experimentally. Note that the forward smoldering velocity values simulated throughout this paper do not exceed at any place the upper bounds observed in the experiments (<1.2 cm/s), thus the expression is not used for extrapolation out of bounds.

The coupling between the three model components – multi-phase flow, front expansion, and calibrated smoldering velocity – is illustrated in Fig. 1. Within a time step, the model first solves Equations (1) and (2) to obtain the relevant hydrogeological parameters – NAPL saturation,  $S_{ij}^{NAPL}$ , and velocity of the air phase (magnitude and direction),  $q_{ij}^{AIR}$  (related to air mass flux ( $\dot{m}_{ij}^{AIR}$ )) – for each discretised block in the domain. These are then employed in Equation (8) to obtain the calibrated forward smoldering velocity,  $V_{ij}^f(t)$ , at each point along the front. Note that all other terms in Equation (8) are constant for a specific fuel and have been determined experimentally by Pironi (2009) or taken from the literature. Variables  $a_{ij}(t)$ ,  $b_{ij}(t)$  and  $c_{ij}(t)$  are then determined via Equations (7a)–(7c) and, along with air flow direction,  $\theta_{ij}(t)$ , are employed to compute the local distances that the front moves via the fully explicit solution to Equations (3) and (4). Loop clipping and regridding of the front, if necessary, occur at this point until all loops are removed and the front is sufficiently resolved. The new position of the front is then mapped to a contiguous array of finite difference nodes in the multiphase flow domain via determining the nearest node centers. The time step is controlled so that the front does not move farther than the width of a single finite difference node in each time step. Finally, NAPL is instantaneously removed from the nodes encompassed by the new smoldering front; the fact that all NAPL is destroyed in the porous media passed

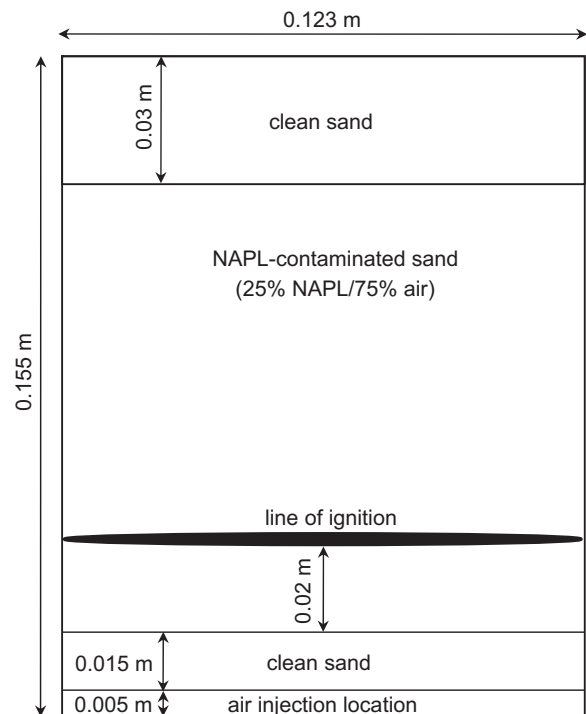


**Fig. 6.** Model set-up for the model domain for the column test simulations.

**Table 4**  
Suite of model testing simulations.

Simulation number	Simulation characteristics
1 (base case)	Homogeneous permeability field Homogeneous NAPL saturation (25%) Single point ignition $\Delta x = \Delta y = 0.0025$ m Front regridding employed
2	Multiple point ignition (3 ignition points)
3	Sensitivity to domain nodal discretization (a) ( $\Delta x = \Delta y = 0.02$ m) (b) ( $\Delta x = \Delta y = 0.01$ m) (c) ( $\Delta x = \Delta y = 0.00125$ m)
4	Effect of front regridding scheme (turned off)
5	Heterogeneous NAPL saturation (dual 25% and 35% regions)
6	Heterogeneous NAPL saturation (regions of varying NAPL saturation)
7	Heterogeneous NAPL saturation (regions with no NAPL)
8	Heterogeneous permeability field (low permeability regions)
9	Heterogeneous permeability field (spatially-correlated random permeability field)

by the smoldering front matches observations in all of the experiments described (Pironi et al., 2011) and the NAPL and air saturations and pressures are subsequently updated in each time step.

### 3. Numerical simulations

#### 3.1. Preliminary simulations

Preliminary simulations were conducted with the ISSM for the column experiments carried out by Pironi et al. (2011) listed in Table 1. The objective was to investigate the capabilities of the ISSM and confirm that the model, calibrated at the local scale, correctly reproduces the experimentally observed global propagation patterns of the smoldering front.

Properties of the coal tar and crude oil samples were measured experimentally for this study and are listed in Table 3. Soil parameters measured by Grant et al. (2007) for N16 sand (WBB Minerals, Brookside Halls, Cheshire, UK) were employed, as its grain size and porosity were similar to those of the Pironi (2009) sand; Table 2 lists the

thermodynamic parameter values employed in the simulation. The model domain used for the column test simulation is presented in Fig. 6.

The simulations assume that the planar domain is consistent with the cross-section along the vertical axis of the column experiments conducted by Pironi et al. (2011). Because the objective of these preliminary simulations is to assess global behavior more than detailed predictions, the plane assumption is acceptable. The model domain was  $0.1225 \text{ m} \times 0.155 \text{ m}$  in the horizontal and vertical directions, respectively. This was discretized into 3038 nodes ( $49 \text{ horizontal} \times 62 \text{ vertical}$ ;  $\Delta x = \Delta y = 0.0025 \text{ m}$ ) as simulations conducted with this nodal dimensions were shown to adequately reproduce the most highly resolved case with the least computational expense (shown in Section 4.2). The multiphase flow equations are self-sharpening and therefore the numerical grid was chosen to be fine enough to optimize excellent mass balance and computational efficiency. The sensitivity of the ISSM to the chosen discretization was informed by a grid sensitivity analysis shown in Section 4.2. The model includes an automatic time adjustment scheme that maximizes  $\Delta t$  but stays within the bounds of conserving mass balance with respect to the non-wetting phase and optimizing the Newton–Raphson iteration scheme. The sides of the domain were assigned no-flow boundaries to both fluids. A fixed air volumetric flux was specified over the bottom boundary, representing the perforated air injection manifold employed (air injection line). At the top of the domain, a fixed air pressure (atmospheric pressure) was applied. For each simulation, an initial NAPL saturation was specified for a  $0.105 \text{ m}$  high layer bounded above and below by clean sand (Fig. 6), reproducing the packing of the column experiments. A line ignition was employed that spans the domain below the contaminated sand, representing the electric heater employed in the experiments. The initial flat ellipse employed to represent the ignition line was very small (vertical thickness of  $0.002 \text{ m}$ ) and therefore only 10 points were required to define it. This corresponds to an initial angular resolution  $\Delta s = 36^\circ$ ; automatic regridding typically resulted in a final  $\Delta s = 1.5^\circ$ . Results are shown in Section 4.

#### 3.2. Model testing simulations

Following model calibration, nine simulations were conducted to test the ISSM's ability to effectively handle two-dimensional

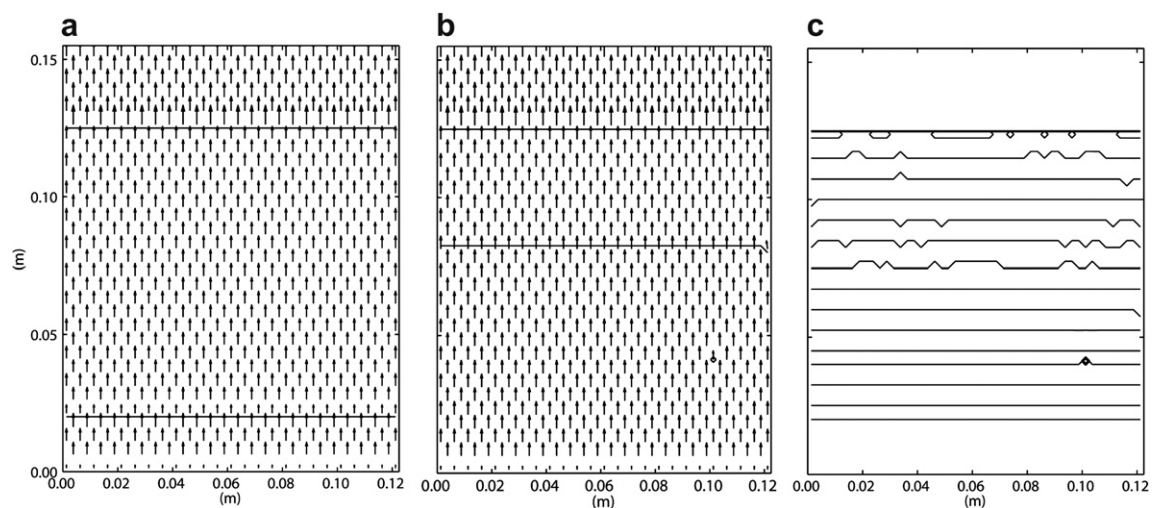


**Fig. 7.** Preliminary simulation, column test case – (a) distribution of air velocity vectors prior to ignition, (b) air velocity vectors (vector size range:  $0.023$ – $0.137 \text{ m/s}$ ) and position of the smoldering front  $625 \text{ s}$  ( $10.4 \text{ min}$ ) following ignition, (c) position of the smoldering front at  $125 \text{ s}$  ( $2.1 \text{ min}$ ) intervals from time  $t = 0 \text{ s}$  (ignition) to  $1175 \text{ s}$  ( $19.6 \text{ min}$ ).



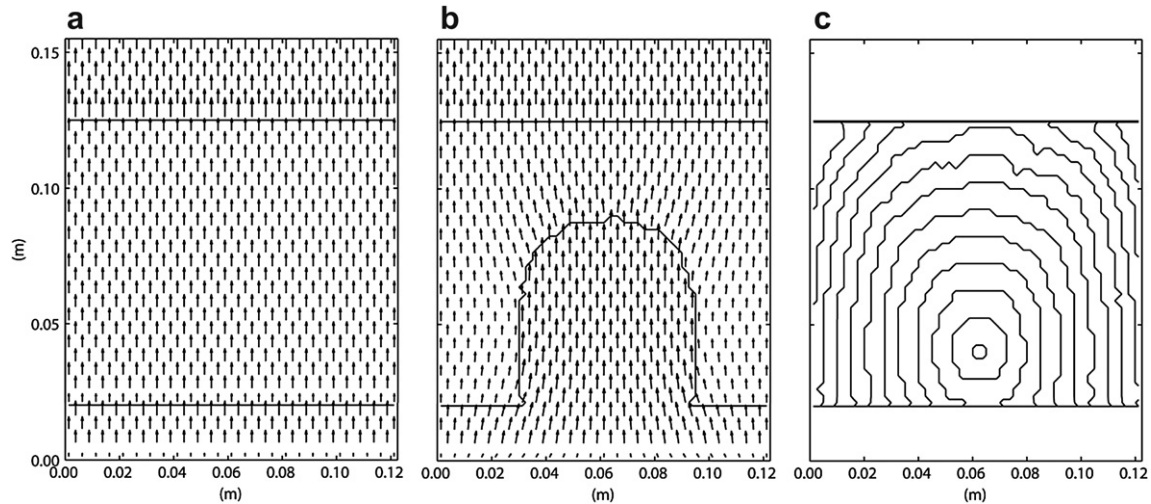


**Fig. 8.** Simulation 1 (base case) – (a) distribution of air velocity vectors prior to ignition, (b) distribution of air (vector size range: 0.022–0.140 m/s) and position of the smoldering front 625 s (10.4 min) following ignition, (c) contour plot of the position of the smoldering front at 125 s (2.1 min) intervals from time  $t = 0$  s to 1500 s (25.0 min).

smoldering propagation, investigate the global smoldering predictions and demonstrate the model's performance for challenging physical scenarios and numerical tests (Table 4). The same model domain as the preliminary simulations (Fig. 6) was employed except that a point ignition (instead of line ignition) was used: front propagation away from a point ignition is a more challenging test. Similar to the preliminary case, an air injection line was employed. For the purposes of this work, “line” is employed to refer to a linear source (of energy or of air) along the width of the 2D domain, while “point” is employed to refer to a single location in the 2D domain. Tables 2 and 3 list the thermodynamic parameter values and the porous medium and fluid properties that were employed. The permeability field, initial and boundary conditions, node number and size match those for Experiment 1 of Table 1 except where noted in Table 4 (further details given in the Results section).

Note that all simulations were conducted on an Intel Core 2 Duo processor, utilized on average 6 MB RAM, and required on average 5 min for each simulation.

## 4. Results and analysis

### 4.1. Preliminary simulations

The base case preliminary simulation (Case 1, Table 1) results are presented in Fig. 7. The air velocity vectors were uniform throughout the solution domain prior to ignition, as expected (Fig. 7a). The air velocity vectors remained fairly uniform during smoldering in this case and the front traversed approximately two-thirds of the 0.105 m contaminated region after 625 s (10.4 min) following ignition (Fig. 7b). The approximately equal distances between front contours illustrate a relatively steady smoldering front velocity with time (Fig. 7c). After 1200 s (20 min), no NAPL remains and the domain is clean, matching experimental results; while NAPL removal is imposed at the local scale by the model, it is important to ensure that this result and the rate of NAPL mass loss are correctly predicted. The global forward velocity of the smoldering front is 0.42 cm/min, which correctly matches the calibration expression value that is applied locally. This value is lower than the experimental velocity of 0.68 cm/

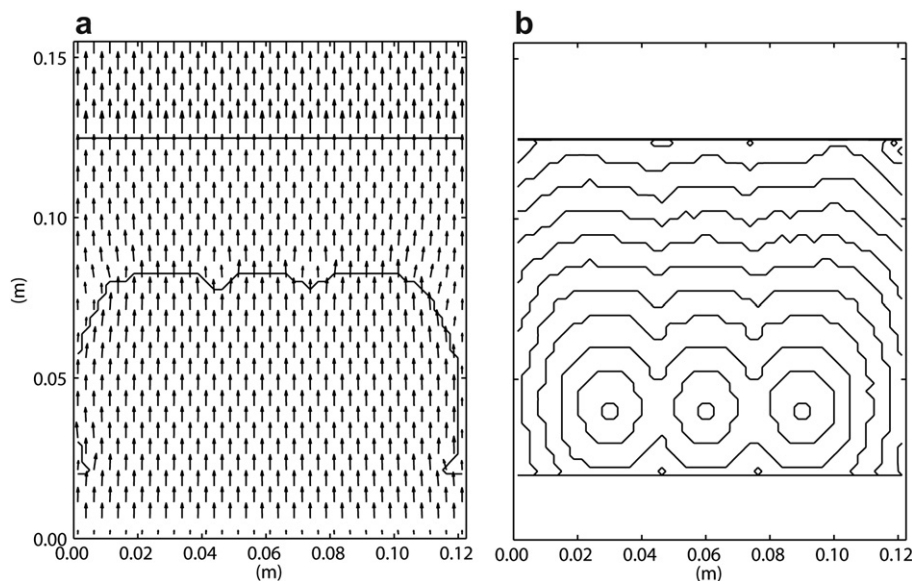


**Fig. 9.** Simulation 2 (multiple ignition scenario) – (a) distribution of air (vector size range: 0.023–0.136 m/s) and position of the smoldering front 625 s (10.4 min) following ignition, (b) contour plot depicting the position of the smoldering front at 125 s (2.1 min) intervals from time  $t = 0$  s to 1500 s (25.0 min).

min due to the difference between the experiment and the calibrated linear expression at this particular air flux value (see Fig. 4, air flux = 9.15 cm/s). Note that the small irregularities in the smoothness of the smoldering front are artefacts of the model coupling interpolation scheme that assigns each point along the front to a node within the finite difference, multiphase flow model grid.

As described in Section 2.3 the calibrated velocity expression is imposed at the local scale (i.e., at each point along the front in the Smoldering Front Expansion Model). Therefore, these results confirmed that the ISSM is able to predict correctly the global behavior of the front advance with time (i.e., propagation patterns and rates in the domain as a whole). Additional simulations of all of the experiments in Table 1 confirm that this conclusion applies across the whole range examined in the published experiments (figures not shown). In these scenarios, it happens that the global velocity is the same as the local velocity because of the homogeneous NAPL saturations, homogeneous porous medium, and uniform air flux. Nevertheless, it is expected that the reliability of the modeling approach applies equally to the more challenging scenarios explored in Section 4.2.

Due to the high viscosity of the coal tar used here (uniform ambient properties assumed), the simulation results show that it is essentially immobile relative to the velocity of the smoldering front. Introduction of the temperature dependency of the viscosity might allow for some NAPL downward migration, but this additional step would be out of the scope of the present proof of concept. It is noted that downward remobilization of coal tar was not observed in the experiments (Pironi et al., 2011).

## 4.2. Model testing simulations

### 4.2.1. Single (base case) and multiple ignition points

The numerical testing base case (Simulation 1, Table 4) is identical to column test calibration simulation (coal tar, air flux of 9.15 cm/s, and NAPL saturation of 25%) except that a point ignition was employed; the point ignition was located 0.02 m above the base of the contaminated layer along the domain midpoint. Simulation 2 is the same as Simulation 1 except that three point ignitions are employed spaced at 0.03 m intervals. Multiple ignition points are an

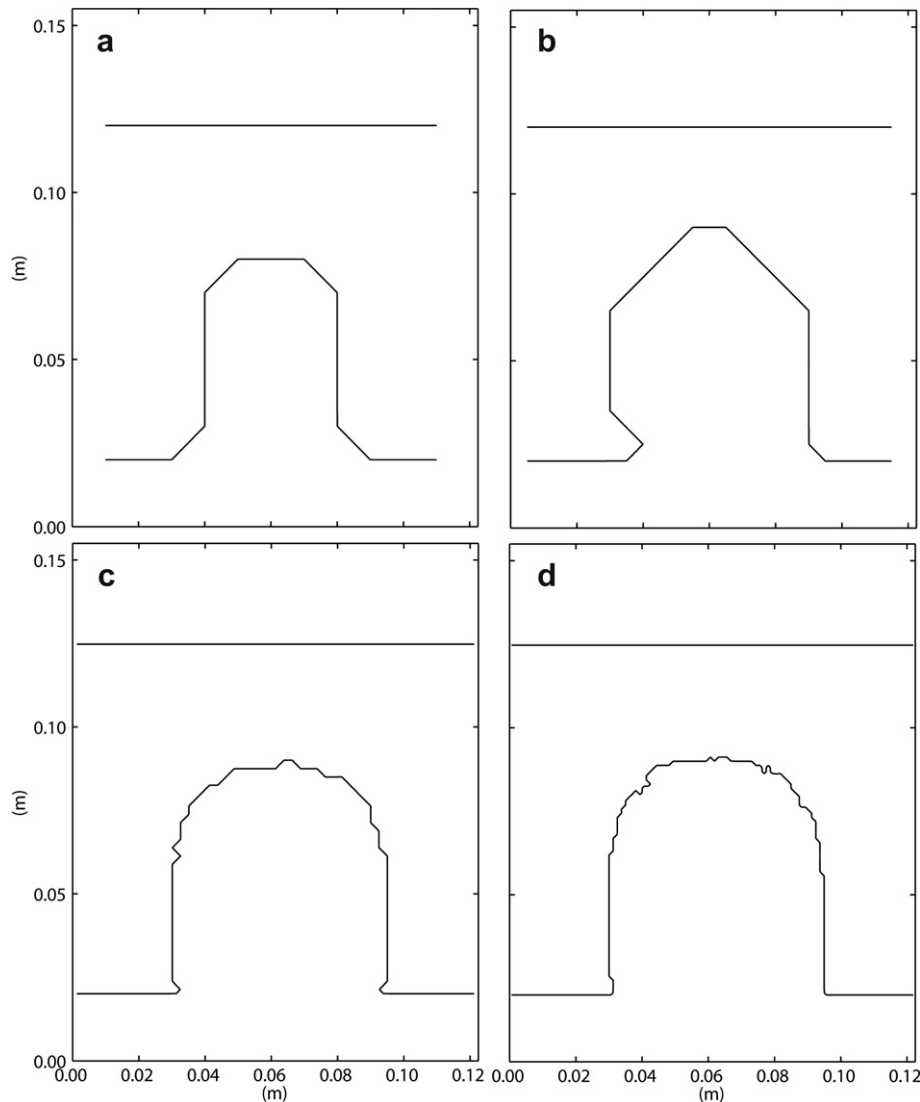


**Fig. 10.** Simulation 3 (sensitivity to nodal discretization) – (a) (Run 3a) number of nodes = 42 ( $\Delta x = \Delta y = 0.02$  m) (b) (Run 3b) number of nodes = 180 ( $\Delta x = \Delta y = 0.01$  m) (c) (Base case) – number of nodes = 3038 ( $\Delta x = \Delta y = 0.0025$  m) (d) (Run 3c) number of nodes = 12,152 ( $\Delta x = \Delta y = 0.00125$  m).

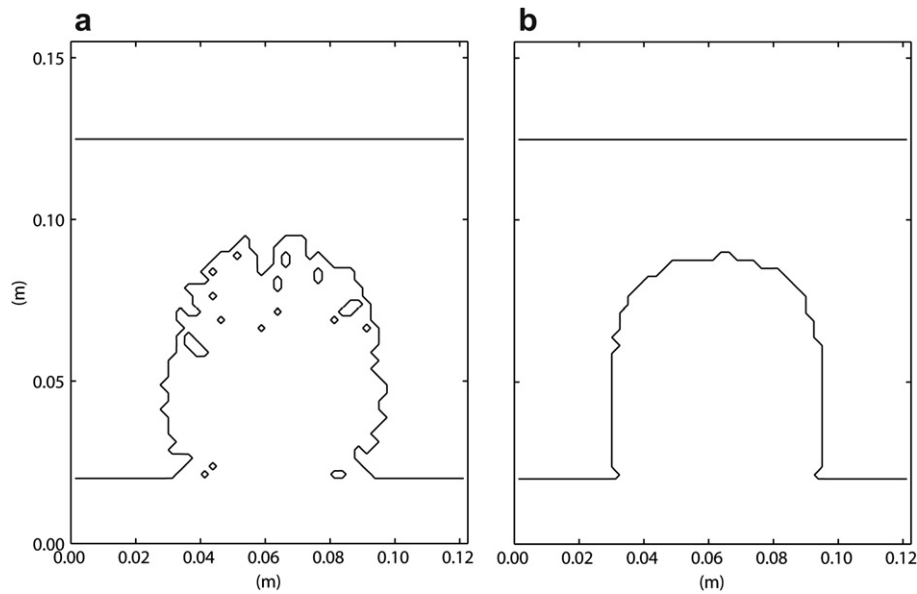


**Fig. 11.** Simulation 4 (effect of front regridding scheme) – (a) smoldering front at 625 s (10.4 min) after ignition without front regridding; number of points defining the front is 360, (b) smoldering front at 625 s (10.4 min) after ignition with front regridding; number of points defining the front is 280.

important test for the model because this is a likely field implementation approach for this process as a remediation technology.

Fig. 8a illustrates that, as expected, the air flux at  $t = 0$  is consistent with previous results (Fig. 7a). Fig. 8b demonstrates that 625 s (10.4 min) after ignition the air flows preferentially through the burnt (i.e., cleaned) section of the domain where the front has passed. This represents a contrast with the line ignition case (Fig. 7) and matches expectations: it is a consequence of the increased effective permeability to the air phase in soil devoid of NAPL. Additionally, the air velocity vectors refract across the combustion front due to the effective permeability contrast; this phenomenon is well known, for example for groundwater flow lines crossing an intrinsic permeability contrast (Domenico and Schwartz, 1998). The distances between contours provide visual representation of the

smoldering front velocity with time (Fig. 8c). As expected, the vertical front velocity is greater than the horizontal velocity. These results match expectations for a two-dimensional forward smoldering front propagation upwards from a single point above a homogeneous air flux line source.

It is noted that the degree of lateral spread depicted in Fig. 8 is sensitive to the assumed lateral spread velocity (Section 2.2). These results employ a lateral spread velocity that is 0.875 times the forward velocity (i.e.,  $\beta = 0.875$ ), and only slight differences in the front propagation pattern is observed for minor deviations of  $\beta$  (e.g.,  $\pm 12.5\%$ ). However a sensitivity simulation with  $\beta \approx 0$  reveals strong differences, with essentially no lateral propagation and the burned zone restricted to a vertical column approximately 2 cm wide centered on the igniter (figures not shown).

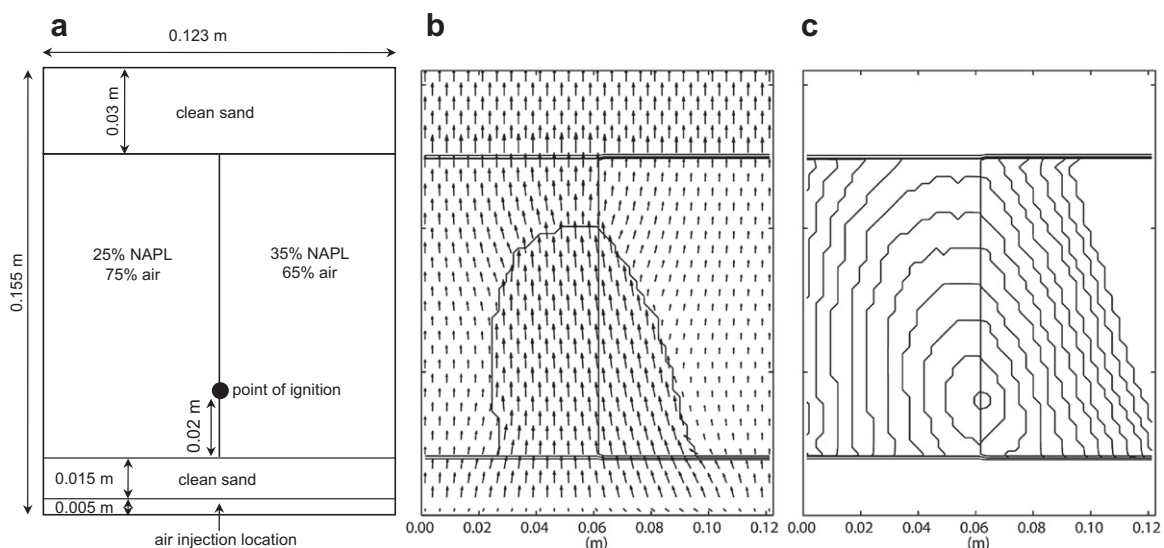


**Fig. 12.** Simulation 5 (25% and 35% dual NAPL saturation) – (a) model domain set-up, (b) distribution of air (vector size range: 0.020–0.169 m/s) and position of the smoldering front 625 s (10.4 min) following ignition, (c) contour plot of the position of the smoldering front at 125 s (2.1 min) intervals from time  $t = 0$  s (ignition) to 1500 s (25.0 min).

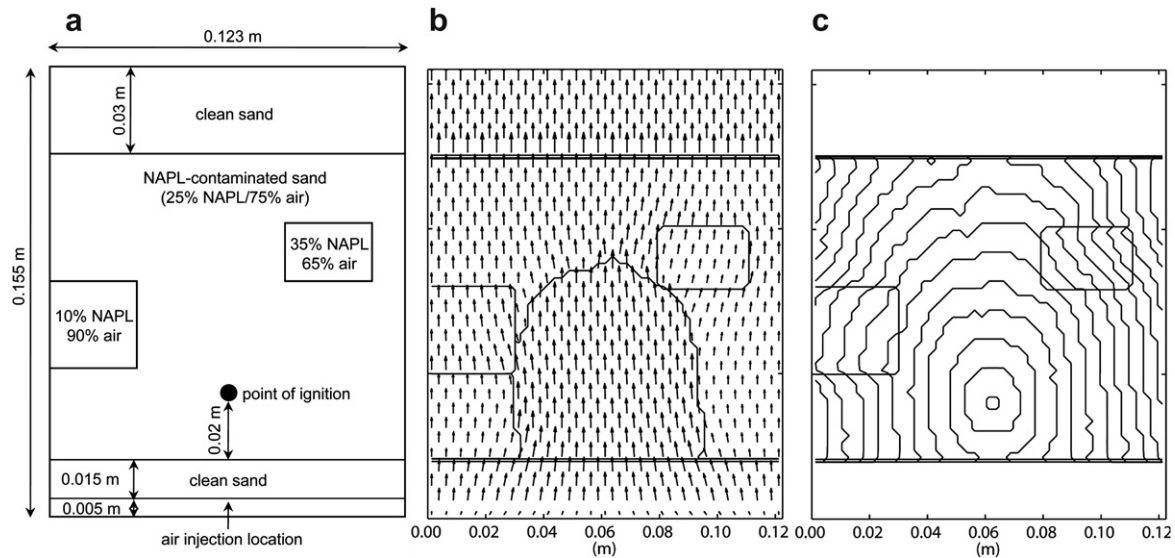


**Fig. 13.** Simulation 6 (variable saturation sections) – (a) model domain set-up, (b) distribution of air (vector size range: 0.022–0.153 m/s) and position of the smoldering front 625 s (10.4 min) following ignition, (c) contour plot of the position of the smoldering front at 125 s (2.1 min) intervals from time  $t = 0$  s to 1500 s (25.0 min).

The multiple ignition sources scenario (Simulation 2) revealed that as the smoldering fronts initiated at each ignition point progress through the domain, they eventually coalesce into one front depicted in Fig. 9a and b. At later time, as expected, the front propagating from multiple ignitions approximates the behavior observed for the line ignition (Fig. 7c).

#### 4.2.2. Sensitivity to domain and front discretization

In Simulations 3a, 3b and 3c, the sensitivity of the base case (Simulation 1) results to the domain nodal discretization is

examined (Table 4). The position of the smoldering front 625 s (10.4 min) after ignition revealed that, as expected, resolution of the front increased with increasing discretization of the finite difference domain (Fig. 10). Computational expense was observed to increase approximately linearly with the number of nodes (simulation time increased 2.5 $\times$ , 35 $\times$ , and 202 $\times$  while the number of nodes increased 4.3 $\times$ , 72 $\times$ , and 289 $\times$  relative to the coarsest case, respectively). Since the simulation with node dimensions of 0.0025 m (Fig. 10c) adequately reproduced the most highly resolved case with 17% of the computational expense, this resolution was chosen for all other simulations.

Simulation 4 is identical to Simulation 1 (base case) except that the front regridding scheme was not turned on. It was revealed that front regridding is an important procedure to avoid the growth of numerical artefacts along the front associated with poor resolution relative to the underlying finite difference domain (Fig. 11). Furthermore, the front regridding scheme increased numerical efficiency, requiring 3% less run time for the base case (Simulation 1) than for the case in which regridding was turned off (Simulation 4).

#### 4.2.3. Heterogeneous NAPL saturation

In Simulation 5, initial NAPL saturations of 25% and 35% were specified in the left and right halves of the domain, respectively (Fig. 12a). All other aspects of the domain were similar to the base case (Simulation 1). Fig. 12b illustrates channeling of a higher fraction of air flowing through the less contaminated section of the domain in Simulation 5 10.4 min after ignition. The embedded relative permeability curves (figure not shown) suggest that an increase from 25% to 35% NAPL saturation would result in an approximate 30% decrease in effective permeability to air. A higher air velocity was also observed through this section, resulting in an increase in the velocity of the front through this region, as expected. Due to the higher NAPL saturations and lower air flow velocities in the right half of the domain it takes longer for this section to be remediated but the smoldering front eventually moves through the entire domain, leaving it NAPL-free.

Simulation 6 is identical to Simulation 1 except that a 0.03 m high by 0.03 m wide section with a NAPL saturation of 10% and a second 0.02 m high by 0.03 m wide section with a NAPL saturation of 35% are emplaced in the solution domain as shown in Fig. 13a.

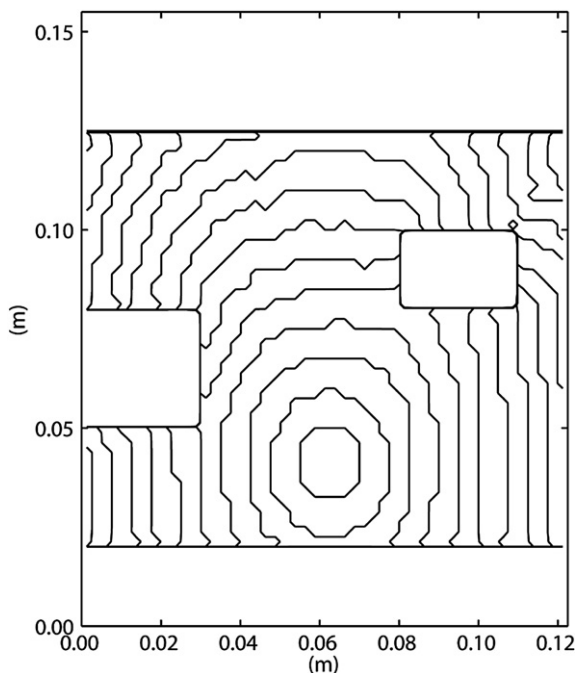


**Fig. 14.** Simulation 7 (regions with 0% NAPL saturation) – contour plot of the position of the smoldering front at 125 s (2.1 min) intervals from time  $t = 0$  s to 1500 s (25.0 min).



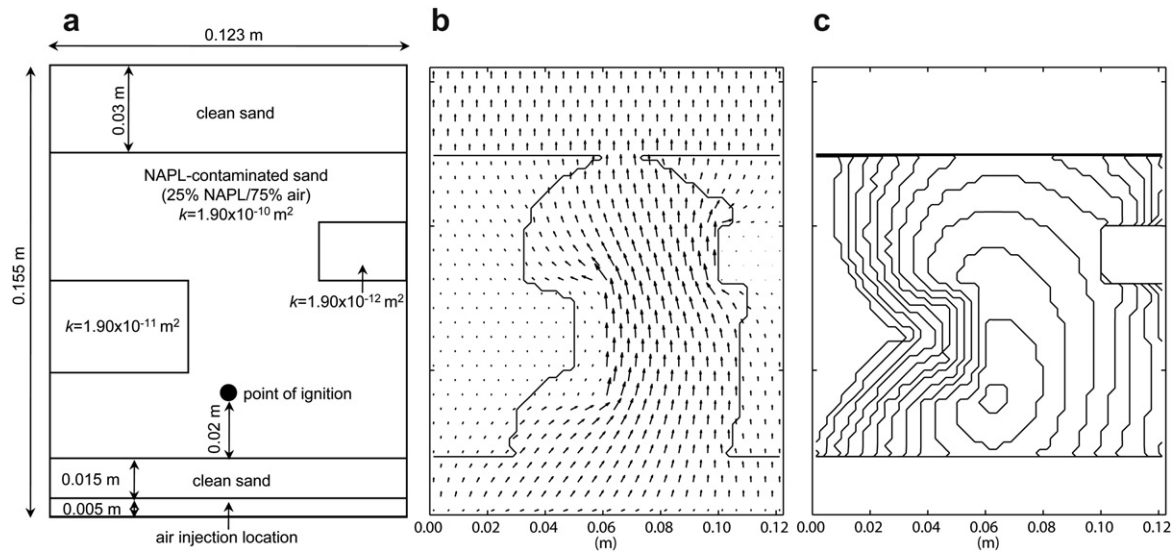


**Fig. 15.** Simulation 8 (low permeability regions): (a) model domain set-up, (b) distribution of air (vector size range: 0.00–0.430 m/s) and position of the smoldering front 625 s (10.4 min) following ignition, (c) contour plot depicting the position of the smoldering front at 125 s (2.1 min) intervals from  $t = 0$  s to 1500 s (25.0 min).

These smaller saturation heterogeneities present an important challenge for the model because field-scale scenarios are expected to have heterogeneities that are small relative to the size of the domain and the full length of front. In Fig. 13b it is observed that air flows preferentially through the section of lower NAPL saturation and is redirected around the section of higher NAPL saturation, as indicated by the air velocity vectors. Fig. 13c is consistent with results previously discussed. As a result of lower air flow velocities due to higher saturation, the velocity of the smoldering front through the 35% NAPL saturation section is much slower than in the other sections while the front moves more quickly through the 10% section relative to the other sections.

Simulation 7 is identical to Simulation 6 except that the two regions exhibit NAPL saturations of 0%. Fig. 14 demonstrates that

the model properly predicted that the front bypasses regions where NAPL is absent and that the smoldering front does not propagate through these regions where the NAPL saturation was less than the critical value of 0.10. It is noted that, by extension, if isolated NAPL-occupied regions were separated by clean (i.e., fuel-free) sand, then each region would have to be contacted by the igniter for smoldering to occur.

#### 4.2.4. Heterogeneous permeability simulations

Simulation 8 employed the same solution domain as the base case Simulation 1 (coal tar, air flux equal to 9.15 cm/s, and a background NAPL saturation equal to 25%) except that a 0.03 m high by 0.03 m wide section with permeability of  $1.9 \times 10^{-11} \text{ m}^2$  (1 order of magnitude reduced from the background) and a second 0.02 m

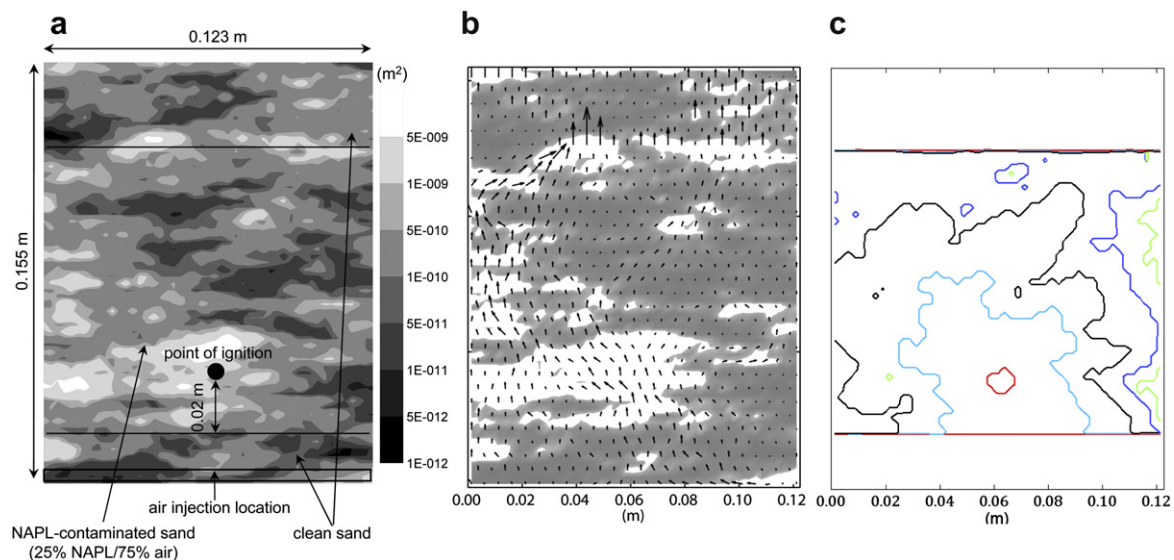


**Fig. 16.** Simulation 9 (small-scale permeability heterogeneity) – (a) model domain set-up; the background grayscale represents the permeability ( $k$ ) field, with the darker shades corresponding to lower  $k$ ; (b) distribution of air prior to ignition (vector size range: 0.00–1.55 m/s); for clarity, the  $k$ -field is represented as a gray/white image in which gray corresponds to  $k < 5 \times 10^{-11} \text{ m}^2$ ; (c) contour plot depicting the position of the smoldering front at 300 s intervals from time  $t = 0$  s to 1500 s.

high by 0.03 m wide section with a permeability of  $1.9 \times 10^{-12} \text{ m}^2$  (2 orders of magnitude reduced from the background) were emplaced in the domain (see Fig. 15a).

Fig. 15 reveals that the velocity of the front, as expected, was reduced proportionally to the effective permeability of the region – in this case the effective permeability contrasts were dictated by the intrinsic permeability rather than the NAPL saturation (as observed for Simulations 5, 6, and 7). In this case, the majority of the air flow and highest front velocities occurred through the center of the domain. Fig. 15c confirms that the smoldering front did not propagate through the lowest permeability region because the air velocity in this block was less than the critical value of 0.5 cm/s. However, the front was able to bypass this region and continued its upward and horizontal propagation in a manner similar to the 0% NAPL saturation case presented above.

In Simulation 9, the effect of small-scale permeability heterogeneities on the shape and velocity of the smoldering front is explored by employing a spatially-correlated, random intrinsic permeability ( $k$ ) field generated via the Turning Bands Method (Mantaglou and Wilson, 1981). The heterogeneous domain was characterized by a horizontal correlation length of 0.0175 m and a vertical correlation length of 0.005 m with a mean permeability of  $k = 4.6 \times 10^{-10} \text{ m}^2$  ( $\ln(k) = -21.5$ ) and a standard deviation of  $\sigma[\ln(k)] = 1.41$  about the mean. This is equivalent to medium sand that is moderately heterogeneous and exhibits horizontal laminations. Correlation lengths were chosen in order to ensure at least 7 correlation lengths are included over the width of the domain and a ratio of horizontal to vertical correlation length of 5:1. The permeability distribution is presented in Fig. 16a in grayscale. An initial, homogeneous NAPL (coal tar) saturation of 25% was specified (irrespective of permeability) for a 0.105 m high section across the entire width of the domain (identical to the base case).

Fig. 16b illustrates the variations in air flow direction and velocity that developed as a result of the small-scale permeability heterogeneities. Fig. 16c reveals that, for Simulation 9, the smoldering front develops a complex shape that reflects the preferential air flow pathways, as expected. Small pockets that did not smolder are also observed behind the front in Fig. 16c. For this figure a distinct color was applied to each contour in order to better illustrate the position of the front and associated pockets at each time step. These sections are associated with bypassing due to excessively low air flux (i.e., low effective permeability). Fig. 16c reveals that the velocity of the front is highly variable, influenced by permeability, NAPL saturation (via relative permeability to air), air flux, air direction, and direction of front propagation.

## 5. Conclusions and summary

The In Situ Smoldering Model (ISSM) was developed through a unique coupling of published models for multiphase flow and combustion front expansion. Embedded was a published analytical expression for the local scale forward smoldering velocity (i.e., at each point along the line that defines the front) as a function of key physical and thermodynamic parameters that was calibrated to 4 unique sets of column experiments. The developed ISSM was demonstrated to predict the global smoldering behavior (extent of propagation, mean front velocity over the whole domain) observed in column tests across a range of NAPL saturations and air fluxes for homogeneous porous media contaminated with coal tar and crude oil.

Numerical testing confirmed that the ISSM modeling approach is numerically stable and computationally efficient. The importance of incorporating a combustion front regridding routine was demonstrated. Testing against challenging two-dimensional problems, for which no experimental data are currently available,

provided confidence that the model is able to handle relatively complex smoldering propagation behavior. Specifically, the ability of the model to handle heterogeneous distributions of NAPL and of intrinsic permeability was demonstrated. As expected, the dominant influence of in situ effective air permeability on smoldering propagation was a prominent theme in the results. Furthermore, the ISSM handled well regions that did not smolder including those with NAPL content and/or air flux values below the required thresholds.

The model takes a phenomenological approach, which provides a practical and computationally efficient tool for exploring in situ smoldering combustion phenomena in natural and engineered systems at a scale not previously possible. It is acknowledged, however, that this approach means the ISSM needs to be calibrated for each fuel type to be simulated. Other limitations of the model include that it applies only to two-dimensional plane domains and thermal front movement, water content and temperature dependence of fluid properties are not currently considered. It is not yet known if the applicability of the model to field-scale scenarios will be limited by these simplifying assumptions; research exploring these questions is underway. Furthermore, the assumptions regarding lateral and opposed propagation rates require validation through additional experiments. Follow-on work will include model validation against multi-dimensional laboratory and field experiments as well as simulations exploring the factors that affect the success of in situ smoldering as a NAPL remediation technique at the field scale.

## Acknowledgments

This research was supported by the Natural Sciences and Engineering Research Council (Canada) and Ontario Centres of Excellence. Smoldering combustion of liquids as a remediation concept is pending patent approval (UK Application 0525193.9 and PCT Application PCT/GB2006/004591, priority date December 2005). The patent is owned by the University of Edinburgh and employed by the University of Western Ontario under license. SiREM/Geosyntec holds an exclusive license to commercialize the STAR (Self-sustaining Treatment for Active Remediation) technology. During this research, Guillermo Rein was a Royal Academy of Engineering/Leverhulme Trust Senior Fellow.

## References

- Akkutlu, I.Y., Yortsos, Y.C., 2003. The dynamics of in-situ combustion fronts in porous media. *Combustion and Flame* 134 (3), 229–247.
- Anderson, H.E., 1983. Predicting Wind-driven Wild Land Fire Size and Shape. US Department of Agriculture, Forest Service. Research Paper (INT 305).
- Aziz, K., Settari, A., 1972. New iterative method for solving reservoir simulation equations. *Journal of Canadian Petroleum Technology* 11 (1), 62–68.
- Bar-Ilan, A., Putzeys, O., Rein, G., Fernandez-Pello, A.C., Urban, D.L., 1972. Transition from forward smoldering to flaming in small polyurethane foam samples. *Proceedings of the Combustion Institute* 30 (2), 2295–2302. doi:10.1016/j.proci.2004.08.233.
- Behie, A., Collins, D., Forsyth Jr., P., 1984. Incomplete factorization methods for three-dimensional non-symmetric problems. *Computer Methods in Applied Mechanics and Engineering* 42 (3), 287–299.
- Coleman, J.R., Sullivan, A.L., 1996. A real-time computer application for the prediction of fire spread across the Australian landscape. *Simulation* 67 (4), 230–240.
- Council, N.R., 2004. Contaminants in the Subsurface: Source Zone Assessment and Remediation. The National Academies Press.
- Domenico, P.A., Schwartz, W., 1998. *Physical and Chemical Hydrogeology*, second ed. Wiley.
- Finney, M.A., 1998. FARSITE: Fire Area Simulator-model Development and Evaluation. USDA Forest Service Publication.
- Gerhard, J.I., Kueper, B.H., 2003a. Capillary pressure characteristics necessary for simulating DNAPL infiltration, redistribution, and immobilization in saturated porous media. *Water Resources Research* 39 (8), SBH71–SBH717.
- Gerhard, J.I., Kueper, B.H., 2003b. Relative permeability characteristics necessary for simulating DNAPL infiltration, redistribution, and immobilization in saturated porous media. *Water Resources Research* 39 (8), SBH81–SBH816.

- Gerhard, J.I., Kueper, B.H., 2003c. Influence of constitutive model parameters on the predicted migration of DNAPL in heterogeneous porous media. *Water Resources Research* 39 (10), SBH41–SBH413.
- Gerhard, J.I., Kueper, B.H., Hecox, G.R., 1998. The influence of waterflood design on the recovery of mobile DNAPLs. *Ground Water* 36 (2), 283–292.
- Gerhard, J.I., Kueper, B.H., Hecox, G.R., Schwarz, E.J., 2001. Site-specific design for dual phase recovery and stabilization of pooled DNAPL. *Ground Water Monitoring and Remediation* 21 (2), 71–88.
- Gerhard, J.I., Pang, T., Kueper, B.H., 2007. Time scales of DNAPL migration in sandy aquifers examined via numerical simulation. *Ground Water* 45 (2), 147–157.
- Grant, G.P., 2005. The evolution of complex DNAPL releases: rates of migration and dissolution. Ph.D. Thesis, University of Edinburgh, Edinburgh, Scotland, UK, 429 pp.
- Grant, G.P., Gerhard, J.I., Kueper, B.H., 2007. Multidimensional validation of a numerical model for simulating a DNAPL release in heterogeneous porous media. *Journal of Contaminant Hydrology* 92 (1–2), 109–128.
- Green, D.G., Gill, A.M., Noble, I.R., 1983. Fire shapes and the adequacy of fire-spread models. *Ecological Modelling* 20 (1), 33–45.
- Green, D.W., 2008. Perry's Chemical Engineers' Handbook.
- Incropera, F.P., DeWitt, D.P., 1996. Introduction to Heat Transfer, third ed. John Wiley & Sons, New York.
- Ji, W., Dahmani, A., Ahlfeld, D.P., Lin Jia, D., Hill, E.I., 1993. Laboratory study of air sparging: air flow visualization. *Ground Water Monitoring and Remediation* 13 (4), 115–126.
- Kashiwagi, T., Nambu, H., 1992. Global kinetic constants for thermal oxidative degradation of a cellulosic paper. *Combustion and Flame* 88 (3–4), 345–368.
- Knight, I., Coleman, J., 1993. A fire perimeter expansion algorithm based on Huggens' wavelet propagation. *International Journal of Wildland Fire* 3 (2), 73–84.
- Kueper, B.H., Frind, E.O., 1991. Two-phase flow in heterogeneous porous media, 1, model development. *Water Resources Research* 27 (6), 1049–1057.
- Kueper, B.H., Gerhard, J.I., 1995. Variability of point source infiltration rates for two-phase flow in heterogeneous porous media. *Water Resources Research* 31 (12), 2971–2980.
- Lord, D.L., Demond, A.H., et al., 2000. Effects of organic base chemistry on interfacial tension, wettability and capillary pressure in multiphase subsurface waste systems. *Transport in Porous Media* 38 (1–2), 79–92.
- Mantaglou, A., Wilson, J.L., 1981. Simulation of Random Fields with the Turning Bands Method. Massachusetts Institute of Technology, Cambridge.
- Marley, M.C., Hazebrouch, D.J., Walsh, M.T., 1992. The application of in-situ air sparging as an innovative soils and ground water remediation technology. *Ground Water Monitoring and Remediation* 12, 137–145.
- McCray, J.E., Falta, R.W., 1997. Numerical simulation of air sparging for remediation of NAPL contamination. *Ground Water* 35 (1), 99–110.
- Ohlemiller, T.J., 1985. Modeling of smoldering propagation. *Progress in Energy and Combustion Science* 11 (4), 277–310.
- Ohlemiller, T.J., 2002. SFPE Handbook of Fire Protection Engineering, pp. 8.
- Pankow, J.F., Cherry, J.A., 1996. Dense Chlorinated Solvents and Other DNAPLs Ground Water. Waterloo Press, Portland (Oregon).
- Philip, J.R., 1998. Full and boundary-layer solutions of the steady air sparging problem. *Journal of Contaminant Hydrology* 33 (3–4), 337–345.
- Pironi, P., Switzer, C., Rein, G., Gerhard, J.I., Torero, J.L., 2009. Small-scale forward smoldering experiments for remediation of coal tar in inert media. *Proceedings of the Combustion Institute* 32 (2), 1957–1964. doi:10.1016/j.proci.2008.06.184.
- Pironi, P., 2009. Smoldering combustion of liquids in porous media for remediating NAPL-contaminated soils. Ph.D. Thesis, University of Edinburgh, Edinburgh, Scotland, UK, 144 pp.
- Pironi, P., Switzer, C., Gerhard, J.I., Rein, G., Torero, J.L., 2011. Self-sustaining smoldering combustion for NAPL remediation: laboratory evaluation of process sensitivity to key parameters. *Environmental Science & Technology* 45 (7), 2980–2986.
- Potter, M.C., Wiggert, D.C., 2001. Mechanics of Fluids.
- Rein, G., 2005. Computational Model of Forward and Opposed Smoldering Combustion with Improved Chemical Kinetics. University of California, Berkeley, 169 pp.
- Rein, G., Lautenberger, C., Carlos Fernandez-Pello, A., Torero, J.L., Urban, D.L., 2006. Application of genetic algorithms and thermogravimetry to determine the kinetics of polyurethane foam in smoldering combustion. *Combustion and Flame* 146 (1–2), 95–108.
- Rein, G., 2009. Smoldering combustion phenomena in science and technology. *International Review of Chemical Engineering* 1 (1), 3–18.
- Rein, G., Fernandez-Pello, A.C., Urban, D.L., 2007. Computational model of forward and opposed smoldering combustion in microgravity. *Proceedings of the Combustion Institute* 31 (2), 2677–2684. doi:10.1016/j.proci.2006.08.047.
- Richards, G.D., 1990. Elliptical growth model of forest fire fronts and its numerical solution. *International Journal for Numerical Methods in Engineering* 30 (6), 1163–1179.
- Richards, G.D., 1993. Properties of elliptical wildfire growth for time dependent fuel and meteorological conditions. *Combustion Science and Technology* 92 (1–3), 145–171.
- Richards, G.D., 1995. A general mathematical framework for modeling two-dimensional wildland fire spread. *International Journal of Wildland Fire* 5 (2), 63–72.
- Richards, G.D., Bryce, R.W., 1995. A computer algorithm for simulating the spread of wildland fire perimeters for heterogeneous fuel and meteorological conditions. *International Journal of Wildland Fire* 5 (2), 73–80.
- Rosenburg, D.U., 1969. Methods for the Numerical Solution of Partial Differential Equations. American Elsevier Pub. Co, New York, 128 pp.
- Switzer, C., Pironi, P., Gerhard, J.I., Rein, G., Torero, J.L., 2009. Self-sustaining smoldering combustion: a novel remediation process for non-aqueous-phase liquids in porous media. *Environmental Science & Technology* 43 (15), 5871–5877.
- Thomson, N.R., Johnson, R.L., 2000. Air distribution during in situ air sparging: an overview of mathematical modeling. *Journal of Hazardous Materials* 72 (2–3), 265–282.
- Torero, J.L., Fernandez-Pello, A.C., 1995. Natural convection smolder of polyurethane foam, upward propagation. *Fire Safety Journal* 24 (1), 35–52.
- Torero, J.L., Fernandez-Pello, A.C., 1996. Forward smolder of polyurethane foam in a forced air flow. *Combustion and Flame* 106 (1–2), 89–109.
- van Dijke, M.I.J., Van Der Zee, S.E.A.T.M., 1998. Modeling of air sparging in a layered soil: numerical and analytical approximations. *Water Resources Research* 34 (3), 341–353.
- van Dijke, M.I.J., van der Zee, S.E.A.T.M., van Duijn, C.J., 1995. Multi-phase flow modeling of air sparging. *Advances in Water Resources* 18 (6), 319–333.
- van Wagner, C.E., 1969. A simple fire growth model. *Forestry Chronicle* 45, 103–104.